ACS APPLIED MATERIALS & INTERFACES
Research Article
www.acsami.org

Copper Doped Hollow Structured Manganese Oxide Mesocrystals with Controlled Phase Structure and Morphology as Anode Materials for Lithium Ion Battery with Improved Electrochemical Performance

Qun Li,[†,‡] Longwei Yin,*[,†] Zhaoqiang Li,[†] Xuekun Wang,[†] Yongxin Qi,[†] and Jingyun Ma[†]

[†]Key Laboratory for Liquid−Solid Structural Evolution and Processing of Materials, Ministry of Education, School of Materials Science and Engineering, Shandong University, Jinan 250061, P. R. China

[‡]College of Chemistry and Chemical Engineering, Taishan University, Tai'an 271021, P. R. China

Supporting Information

ABSTRACT: We develop a facile synthesis route to prepare Cu doped hollow structured manganese oxide mesocrystals with controlled phase structure and morphology using manganese carbonate as the reactant template. It is shown that Cu dopant is homogeneously distributed among the hollow manganese oxide microspherical samples, and it is embedded in the lattice of manganese oxide by substituting Mn^{3+} in the presence of Cu^{2+}. The crystal structure of manganese oxide products can be modulated to bixbyite Mn_2O_3 and tetragonal Mn_3O_4 in the presence of annealing gas of air and nitrogen, respectively. The incorporation of Cu into Mn_2O_3 and Mn_3O_4 induces a great microstructure evolution from core−shell structure for pure Mn_2O_3 and Mn_3O_4 samples to hollow porous spherical Cu-doped Mn_2O_3 and Mn_3O_4 samples with a larger surface area, respectively. The Cu-doped hollow spherical Mn_2O_3 sample displays a higher specific capacity of 642 mAhg^{-1} at a current density of 100 mA g^{-1} after 100 cycles, which is about 1.78 times improvement compared to that of 361 mA h g^{-1} for the pure Mn_2O_3 sample, displaying a Coulombic efficiency of up to 99.5%. The great enhancement of the electrochemical lithium storage performance can be attributed to the improvement of the electronic conductivity and lithium diffusivity of electrodes. The present results have verified the ability of Cu doping to improve electrochemical lithium storage performances of manganese oxides.

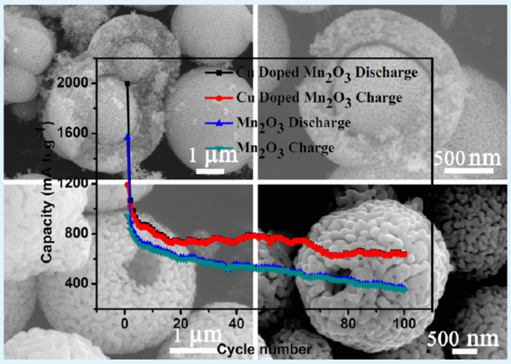

KEYWORDS: *manganese oxide, doping, core−shell structure, hollow structure, lithium ion battery, anode material*

1. INTRODUCTION

Electrical energy storage is becoming a more and more important issue with the development of industry and society. Currently, lithium ion batteries (LIBs) have been widely used in many portable electronic devices, such as mobile phones, laptops, and cameras, due to their high energy density, high rate capability, high safety, and low cost.[1,2] Graphite-based materials are generally used as anode materials in commercial LIBs. However, as anode material for LIBs, graphite is limited by its low theoretical specific capacity of 372 mA h g^{-1} and limited rate capability. Transition metal oxides with higher energy density (such as MnO_x,[3−6] Fe_2O_3,[7] Co_3O_4,[8] NiO,[9] $CoFe_2O_4$,[10] and $ZnCo_2O_4$[11]) have drawn much attention as the desired candidates for anode materials to satisfy the higher energy storage requirements.[12] Among these transition metal oxides, manganese oxide is of great importance as anode materials for LIBs due to its low operating voltage, low toxicity, low cost, and widespread availability.[4,13,14]

However, the implementation of manganese oxide in rechargeable LIBs is still largely hampered by some practical problems, such as poor cycling performance and poor electronic conductivity.[1,15] In terms of metal oxide anode materials, the poor cycling performance problem is common, and has been known to result from the large specific volume change formed during lithiation and delithiation cycling. Much attention has been paid to accommodate transformation strains upon continuous cycling and improve the poor capacity retention. One promising strategy is to design nanostructured manganese oxide-based anode materials, such as nanofilms,[3] nanotubes,[4] hollow spheres,[5,14] and nanofibers.[16] Taking into consideration the ability of the hollow nanostructure to suppress volume changes and resulting pulverization, micro- or submicrometer-sized hollow and/or porous materials are attracting increasing attention among researchers and scientists.

The electrochemical performance of the electrode materials could be further enhanced by increasing electrical conductivity by making nanocomposite materials with carbon,[13,16−18] or altering the inherent conductivity via lattice doping using some other transition metal ions. Particularly, cationic doping has been certified to be an effective means to improve the electrical

Received: August 5, 2013
Accepted: September 30, 2013
Published: September 30, 2013

dx.doi.org/10.1021/am403215j | *ACS Appl. Mater. Interfaces* 2013, 5, 10975−10984

conductivity and charge transfer ability of the anode materials. Prompted by these interests, various metal cations (such as antimony,[19] niobium,[20] tantalum,[21] cobalt,[15,22] and copper[23−25]) have been consumingly used to improve electrochemical performance of metal oxide anode materials. Previous investigations have showed that cation doped materials exhibit remarkably enhanced electrochemical performance. Copper, with the second highest electrical conductivity while being much cheaper, exposes itself as one of the most advisable candidates for cationic doping.

Recently, much attention has been paid to the application of manganese oxides as anode materials in LIBs, and much effort has been made to control the structure of manganese oxides to enhance the performance of the anode materials. As is known, the porous structure not only increases the energy density, but also improves the cycle performance. One of the appealing methods to obtain the porous structure is to in situ thermally decompose the metal carbonates, hydroxides, or carbonate-hydroxides precursors. Qiu et al.[26] prepared oval-shape and straw-sheaf-shape Mn_2O_3 hierarchical structure through a hydrothermal chemical route using functional polyol molecules and potassium permanganate as precursors, and investigated the effect of the nanostructured Mn_2O_3 anode materials on the electrochemical lithium storage performance during Li^+ insertion/extraction cycling. It is shown that the straw-sheaf-shaped Mn_2O_3 displayed a high specific capacity of above 380 mA h g^{-1} after 150 cycles. Shim and co-workers developed the hollow rod-like manganese oxides using bacterial templates, exhibiting a high specific capacity up to about 300 mA h g^{-1} after 10 cycles.[27] Up to now, a variety of methods (such as biomineralization, molten salt method, and bacterial soft template method) have been utilized to prepare manganese oxide electrode materials. However, most of these complicated synthetic procedures are commonly low-yield, high-cost, and time-consuming. To the best of our knowledge, structure-controlled synthesis of doped hollow structured manganese oxide materials by metallic doping has been challenging.

Herein, we developed a facile synthesis route to prepare Cu-doped hollow structured manganese oxide mesocrystals with controlled phase structure and morphology using manganese carbonate as the reactant template. Cu dopant is homogeneously distributed among the hollow manganese oxide microspherical samples and embedded in the lattice of manganese oxide by substituting Mn^{3+} in the presence of Cu^{2+}. The incorporation of Cu into Mn_2O_3 and Mn_3O_4 induces a great microstructure evolution from core−shell structure for pure Mn_2O_3 and Mn_3O_4 samples to hollow porous spherical Cu-doped Mn_2O_3 and Mn_3O_4 samples with a larger surface area, respectively. The Cu-doped hollow spherical Mn_2O_3 sample displays a higher specific capacity of 642 mA h g^{-1} at a current density of 100 mA g^{-1} after 100 cycles, which is about 1.78 times than that of 361 mA h g^{-1} for pure Mn_2O_3 sample, displaying a Coulombic efficiency of up to 99.5%. The present results have verified the ability of Cu doping to improve electrochemical lithium storage performances of manganese oxides.

2. EXPERIMENTAL SECTION

2.1. Material Synthesis. The manganese oxide microspheres were synthesized by thermally annealing $MnCO_3$ precursors in the presence of air and nitrogen gas flow, respectively. All of the reactants and solvents are from Shanghai Chemical Co. Ltd., China. In this work, all chemical reagents are analytical grade and are used without further purification. In a typical synthesis, 0.01 mol of manganese acetate tetrahydrate, 0.005 mol of copper chloride dihydrate, and 0.09 mol of urea were added into 35 mL of ethylene glycol to form the solution. The resultant mixture was continually stirred for 2 h and then transferred into a 100 mL Teflon-lined stainless-steel autoclave. The Teflon-lined autoclave was put into an oven at 180 °C for 24 h. The system was then cooled to ambient temperature naturally. The final product was collected and washed with distilled water and absolute alcohol at least five times. The as-synthesized samples were further annealed at 600 °C with a temperate rate of 2 °C min^{-1} and kept at the same temperature for 10 h in air.[7,28] The synthesis of pure manganese oxides were the same as those above-mentioned but without copper chloride dihydrate.

2.2. Structure Characterization. The crystal structure information of the synthesized samples was established by powder X-ray diffraction (XRD, Rigaku D/Max-KA diffractometer with Cu Ka radiation). SU-70 field emission scanning electron microscopy (FESEM) was employed to analyze the morphology, and the chemical components of the products were measured with an energy dispersive X-ray spectrometer (EDS). The microstructures of the synthesized products were observed by high-resolution transmission electron microscopy (HRTEM JEM-2100). X-ray photoelectron spectroscopy (XPS, ESCALAB 250 with 150 W Al Ka probe beam) was used to characterize the chemical composition information. The specific Brunauer−Emmett−Teller (BET) surface area was determined by N_2 adsorption/desorption on a V-Sorb 2800 series analyzer (Gold APP Co. Ltd.).

2.3. Electrochemical Characterization. The electrochemical measurements were conducted using standard 2025 type coin cells with copper foil as the current collectors, lithium foil as counter electrode and reference electrodes and 1.0 M $LiPF_6$ in a 1:1 (V/V) mixture of ethylene carbonate (EC) and diethyl carbonate (DEC) as the electrolyte. The cutoff voltage window is 0.01−3.0 V. The working electrode mixture slurry was prepared by mixing 70 wt % active materials, 20 wt % acetylene carbon black, 10 wt % polyvinylidene fluoride (PVDF) binder, and an adequate amount of *N*-methyl-2-pyrrolidone (NMP). Galvanostatically cycled test was carried out on a LAND CT2001A instrument (Wuhan, China) at room temperature. Electrochemical workstation (PARSTAT2273) was used to study cyclic voltammetry (CV) test in a potential window of 0.01−3.0 V at a scan rate of 0.1 mV s^{-1}.[13]

3. RESULTS AND DISCUSSION

3.1. Structure Characterization of Mn_2O_3 Samples. The powder XRD patterns of the as-synthesized products are shown in Figure 1. The $MnCO_3$ precursors with rhodochrosite strucuture (JCPDS card No. 44-1472) were first synthesized via a solvethermal reaction route. Figure 1a depicts the XRD pattern of synthesized $MnCO_3$ precursors. From Figure 1b of the XRD pattern of the products obtained after annealing $MnCO_3$ precursors in air, it indicates that pure Mn_2O_3 (JCPDS: 41-1442) sample with bixbyite structure (space group $Ia\overline{3}(206)$) can be obtained.

The XRD pattern of the Cu-doped manganese oxide sample shown in Figure 1b is basically in agreement with that of bixbyite Mn_2O_3, except for the intensity of some diffraction peaks becomes stronger compared with that of pure Mn_2O_3. Furthermore, the diffraction peaks shift right to the positions at large angles, indicating that the incorporation of Cu into lattice of bixbyite Mn_2O_3 results in the decrease of the lattice constant of Mn_2O_3. Figure 1c depicts the XRD patterns of magnified (222) peak of pure and Cu-doped Mn_2O_3 sample, clearly showing that (222) peak shifts to a position at higher angle. The lattice parameters of the pure Mn_2O_3 sample and Cu-doped Mn_2O_3 samples can be calculated through the Bragg equation from the diffraction peaks of (222), (400), (431), and (440). The lattice constant is 9.4226 Å for the pure Mn_2O_3

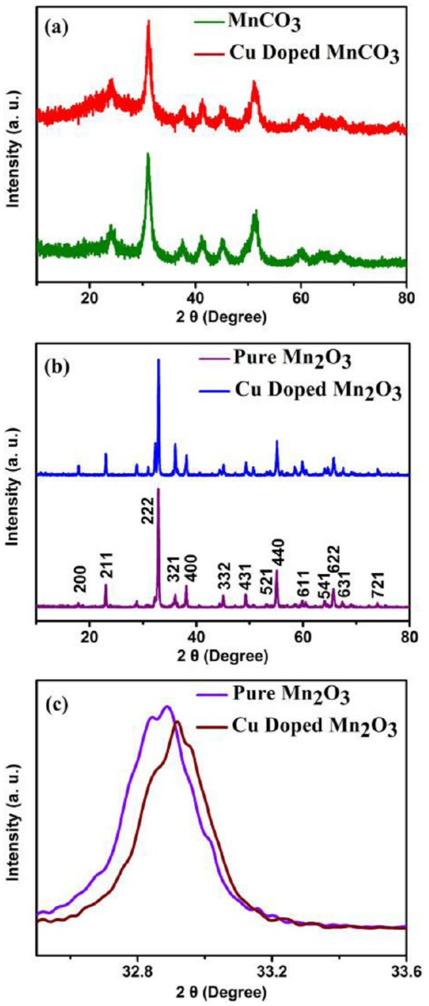

Figure 1. XRD patterns of the samples. (a) $MnCO_3$ and Cu-doped $MnCO_3$, (b) Mn_2O_3 and Cu-doped Mn_2O_3, and (c) magnified (222) peak of pure Mn_2O_3 and Cu-doped Mn_2O_3 samples.

sample and 9.4152 Å for the Cu-doped Mn_2O_3 sample. The reason for the Cu incorporation into Mn_2O_3 causing the decrease in lattice constant is due to the smaller radius of the Cu^{2+} ion (0.057 nm) than that of the Mn^{3+} (0.066 nm) ion.[29]

In order to obtain the further information about the chemical composition and the chemical bonding state of Cu-doped Mn_2O_3, we further carried out characterization via X-ray photoelectron spectroscopy (XPS) study, as shown in Figure 2. Figure 2a displays the overall XPS spectrum for peaks of Mn (Mn $2p_{1/2}$, Mn $2p_{3/2}$, Mn 3p), O (O 1s), and Cu (Cu 2p). Figure 2b depicts a high-resolution XPS spectrum of Mn 2p, where two peaks located at 641.9 and 653.45 eV can be attributed to Mn $2p_{3/2}$ and Mn $2p_{1/2}$ levels, respectively. The spin energy separation is about 11.55 eV, which is smaller than the spin energy separation of 11.7 eV of standard Mn_2O_3.[30] It is believed that the Cu doping may be the reason for the presence of small spin energy separation compared with that of pure Mn_2O_3. From previous reports, the spin energy separation of Mn_2O_3 is in a range of 11.4 to 11.7 eV.[28,31] The present result is in agreement with this range. From XPS spectrum (Figure 2c) of the deconvoluted O 1s, it suggests that three peaks locate at 529.35, 530.5, and 531.4 eV, indicating that the oxygen in this sample is present in the form of oxide.[21,28] The XPS spectrum of the Cu 2p peak shown in Figure 2d suggests that the intensity of the peak is very weak. Two peaks located at 933.8 and 953.5 eV can be attributed to Cu $2p_{3/2}$ and Cu $2p_{1/2}$ levels, which is similar to that reported in the CuO sample.[32] It is indicated that Cu is incorporated into the lattice of Mn_2O_3 in the form of bivalence (Cu^{2+}). This is in agreement with the XRD analysis result. As indicated by the XRD pattern in Figure 1b, the XRD pattern of Cu-doped Mn_2O_3 is basically in agreement with that of bixbyite Mn_2O_3. No XRD peaks related to copper oxide could be found. The lattice constant of 9.4226 Å for the pure Mn_2O_3 sample is larger than the lattice constant of 9.4152 Å for the Cu-doped Mn_2O_3 sample, indicating that the incorporation of Cu into lattice of bixbyite Mn_2O_3 results in the decrease of the lattice constant of Mn_2O_3.

FESEM was used to study the morphology of the synthesized products. Figure S1 in the Supporting Information shows the FESEM images of the as-prepared carbonate precursor template. As shown in Figure S1, the synthesized $MnCO_3$ is spherical particle with a smooth surface, with a size distribution from 3 to 4 μm. It is shown that Cu-doped $MnCO_3$ microspheres are more uniform than the pure $MnCO_3$ microspheres.

Figure 3a shows the FESEM images of pure Mn_2O_3 microspheres obtained via thermal annealing under air. From low magnification FESEM image of the synthesized Mn_2O_3 samples in Figure 3a, it is shown that synthesized products display spherical morphology, with a uniform size distribution ranging from 3 to 5 μm. The interior microstructures of the synthesized Mn_2O_3 spheres can be revealed by the FESEM images of broken spheres. Figure 3b−f gives magnified FESEM images of the spherical Mn_2O_3 samples collapsed or broken, clearly showing core−shell characteristic structure for the synthesized spherical Mn_2O_3 samples. The spherical core−shell Mn_2O_3 samples are actually composed of nanoparticles with an average size of 30−40 nm. The core is about 1−2 μm, and the shell is about 400−800 nm in width. From Figure 3f, it is clearly demonstrated that the shell of the core−shell Mn_2O_3 spheres even contains several separated layers. Figure S2 gives a typical EDS spectrum of pure Mn_2O_3 samples, suggesting the synthesized products are composed of Mn and O elements.

The incorporation of Cu into lattice of Mn_2O_3 plays a greatly important role on the structure, porous nature, and surface area of the synthesized products. The Cu-doped Mn_2O_3 samples display a completely distinct morphology compared with pure Mn_2O_3 samples (Figure 4). Figure 4a shows a low magnification SEM image of the Mn_2O_3 sample. It clearly demonstrates that the Cu-doped Mn_2O_3 microspheres are more uniform in size distribution than the pure Mn_2O_3 spherical samples. Figure 4b and c depicts the high magnification SEM images of Cu-doped Mn_2O_3 sample, showing that the spherical Mn_2O_3 samples are formed by self-assembly of Cu-doped Mn_2O_3 nanoparticles with an average size of 100−200 nm. SEM images of several Cu-doped Mn_2O_3 spherical samples with an open mouth (Figure 4d−f) reveal that the hollow nature of the Cu-doped Mn_2O_3 spherical samples. Figure 5 gives a typical EDS spectrum of Cu-doped Mn_2O_3 samples, suggesting the synthesized products are composed of Mn, O, and Cu elements, and these three elements are homogeneously distributed among the whole products.

Transmission electron microscopy (TEM) was used to further investigate the detailed microstructures of the synthesized mesocrystals Mn_2O_3 materials (Figure 6). From the TEM images in Figure 6a and b for Mn_2O_3 and Cu-doped Mn_2O_3, respectively, it is shown that the Mn_2O_3 hierarchical

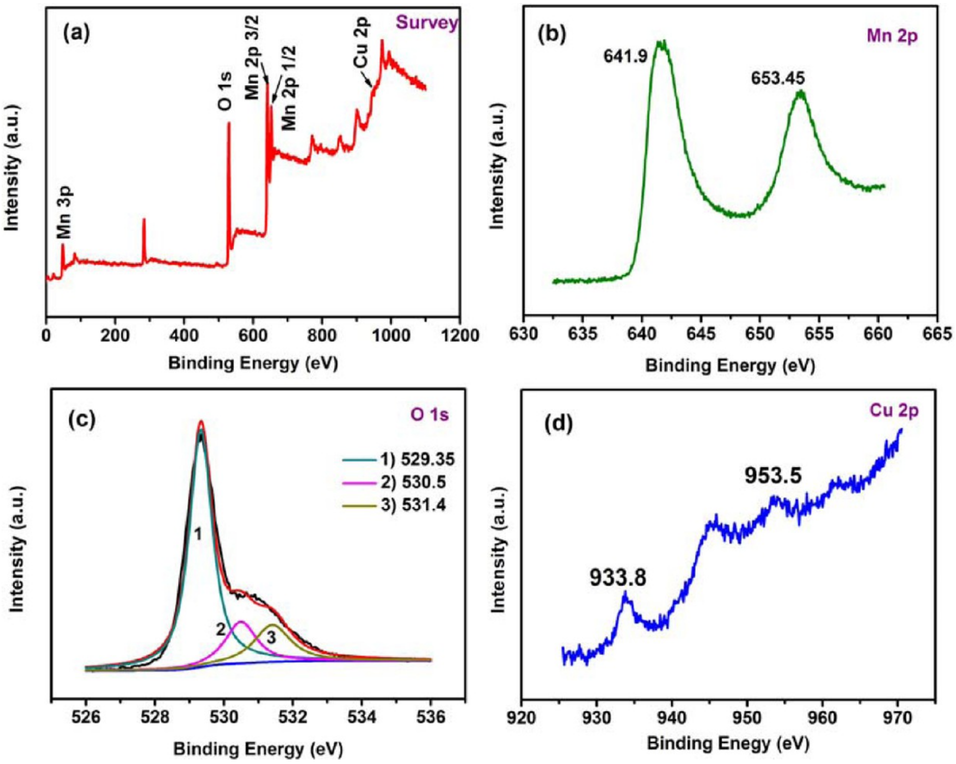

Figure 2. XPS spectra of Cu-doped Mn_2O_3 microsphere. (a) Survey spectrum, (b) Mn 2p, (c) O 1s, and (d) Cu 2p.

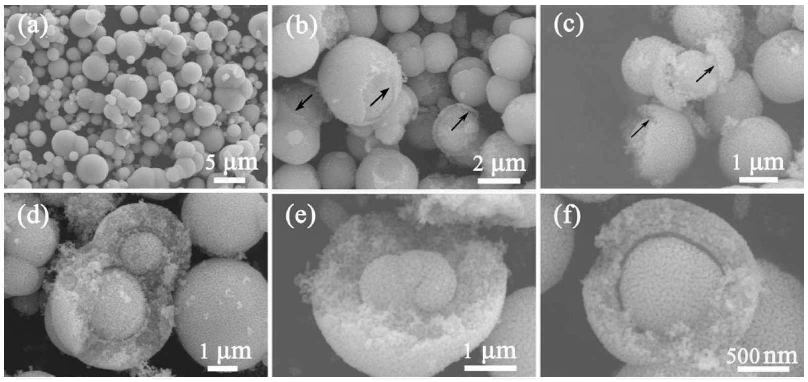

Figure 3. SEM images of pure Mn_2O_3 core−shell microsphere samples: (a) low magnification and (b−f) high magnification.

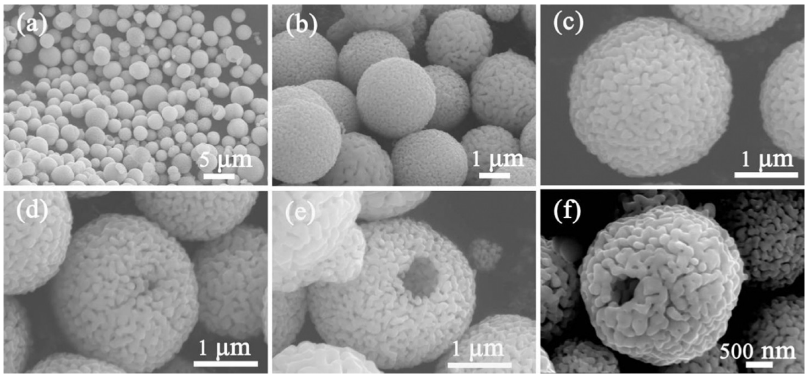

Figure 4. SEM images of Cu-doped Mn_2O_3 hollow microsphere samples: (a) low magnification and (b−f) high magnification.

spherical samples are composed of small nanoparticles. The core−shell structure for pure Mn_2O_3 and hollow structure for Cu-doped Mn_2O_3 structure cannot be directly revealed, because the shell width of spherical samples is larger. The crystal structural of the samples was determined according to the selected area electron diffraction (SAED) pattern shown in

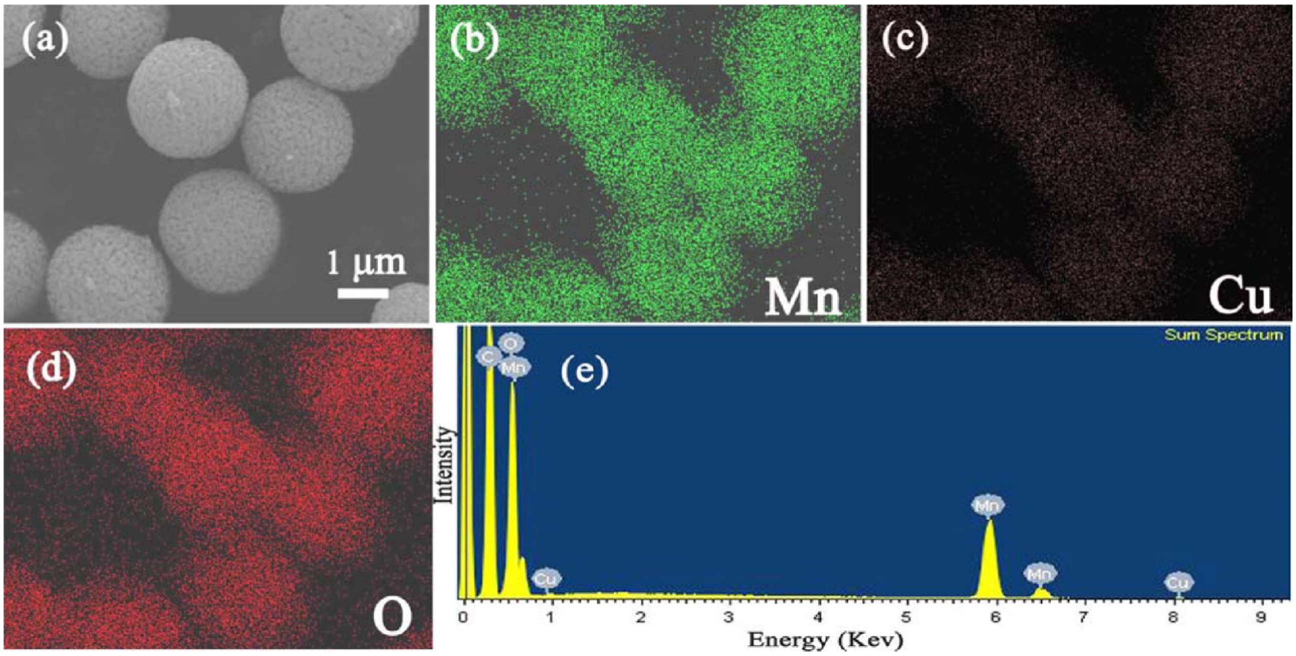

Figure 5. (a) SEM image. (b) Mn, (c) Cu, and (d) O elemental mapping images of Cu doped Mn_2O_3 microsphere. (e) EDS spectrum of Cu doped Mn_2O_3 microsphere.

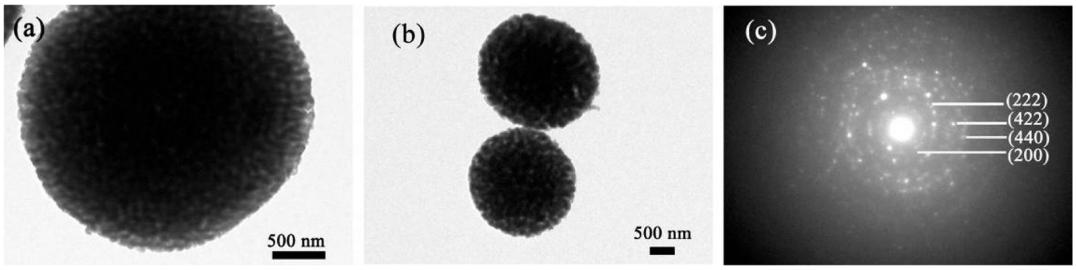

Figure 6. TEM images of (a) pure Mn_2O_3 samples and (b) Cu doped Mn_2O_3 samples. (c) SAED patterns of the pure Mn_2O_3 samples.

Figure 6c, suggesting a polycrystalline nature for the synthesized bixbyite Mn_2O_3. The diffraction rings in Figure 6c correspond well with the (200), (222), (422), and (440) planes of bixbyite structured Mn_2O_3.

The formation mechanism of the pure core–shell Mn_2O_3 microsphere and hollow structured Cu-doped Mn_2O_3 spherical samples are shown in Figure 7. The formation process of the core–shell structure during the thermal decomposition of $MnCO_3$ is mainly based on the heterogeneous contraction caused by the nonequilibrium heat treatment process. First, at the initial stage of calcination, the Mn_2O_3 thin shell was formed on the surface of $MnCO_3$ core because of a large temperature gradient along the radial direction. As the temperature reaches 600 °C, the inner $MnCO_3$ core began to decompose to form the Mn_2O_3 core, and is separated from the outer shell during the continuing calcination, and the core–shell Mn_2O_3 microsphere formed finally.[11,28]

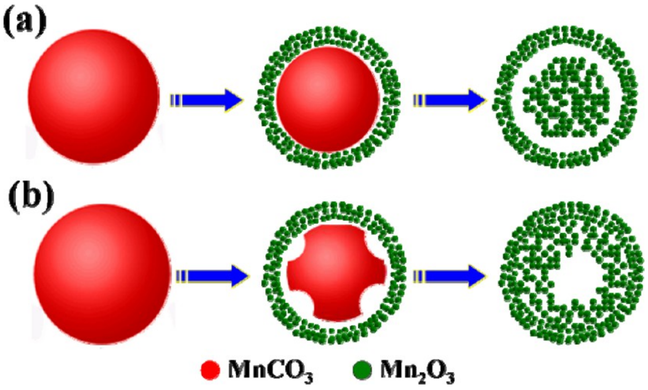

Figure 7. Schematic illustration of the formation process of (a) core–shell structure Mn_2O_3 samples and (b) hollow structure Cu doped Mn_2O_3 microsphere.

As for the hollow structure of Cu-doped Mn_2O_3 microspheres, it is assumed that the formation of micrometersized hollow spheres is analogous to that reported previously.[33,34] It can be explained as a fundamental solid-state phenomenon, the so-called Kirkendall effect,[28,34] which deals with the movement of the interface between diffusion couples. Under continuous thermally annealing in the presence of air gas flow, Cu-doped $MnCO_3$ spherical crystals can decompose to form a diffusion pair of Cu-doped Mn_2O_3 (It is noted that Cu-doped Mn_3O_4 can be formed from the decomposition of Cu-doped $MnCO_3$ in the presence of nitrogen gas). The coupled reaction/diffusion at the Cu-doped $MnCO_3/Mn_2O_3$ interface might lead to the quick formation of a layer of Cu-doped Mn_2O_3 shell around the outside surfaces of the Cu-doped $MnCO_3$ crystals. The directly continuous conversion of core Cu-doped $MnCO_3$ material to

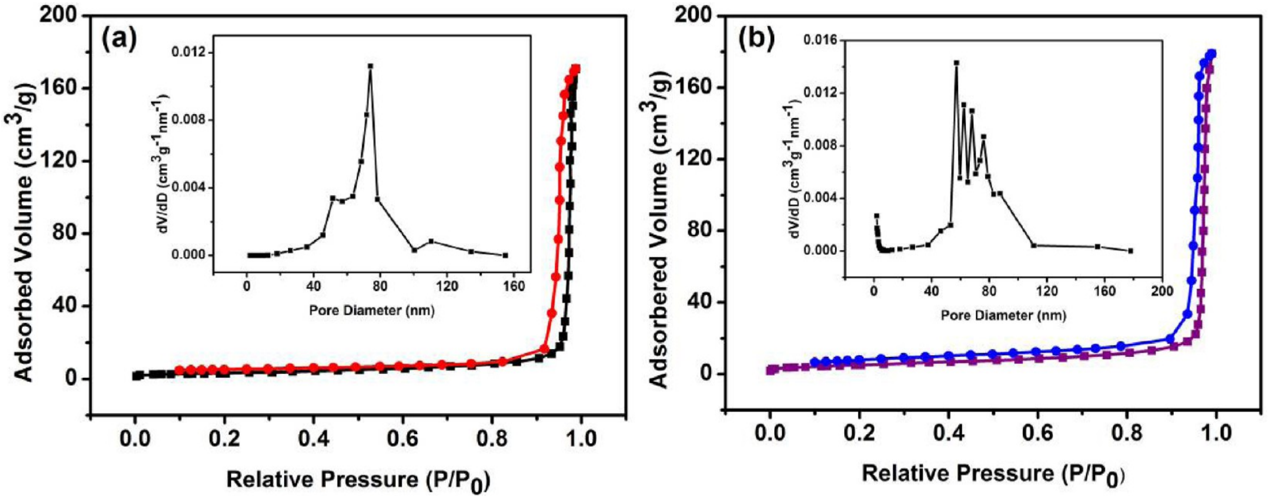

Figure 8. Nitrogen adsorption−desorption isotherms and the corresponding pore size distribution for samples: (a) pure Mn_2O_3 sample and (b) Cu doped Mn_2O_3 sample.

Cu-doped Mn_2O_3 shell material is therefore hindered by the layer and further reaction will continue by the diffusion of atoms or ions through the interface. The nonequilibrium interdiffusion between the Cu-doped Mn_2O_3 from Cu-doped $MnCO_3$ results in a net material flux across the interface layer and simultaneously causes a flow of fast-moving vacancies to the vicinity of the solid−solid interface. Therefore, the hollow Cu-doped Mn_2O_3 microspheres are formed through coalescence of the vacancies based on the Kirkendall effect.[28,35−38]

The nitrogen adsorption−desorption isotherms and the corresponding pore size distribution curves by the Barrett−Joyner−Halenda (BJH) method of the pure Mn_2O_3 and Cu-doped Mn_2O_3 samples are shown in Figure 8. The two kinds of spherical samples exhibit a typical type IV characteristic with an obvious capillary condensation step, indicating that the mesoporous nature of the synthesized M_2O_3 spherical smaples.[28] The hysteresis loop shown in isotherms is very narrow and small, indicating that the presence of macroporous in the samples. For the pure Mn_2O_3 sample, the pores are in a range of 40−90 nm, with an average pore size of 75 nm. The specific surface area and the pore volume are calculated to be 11.58 m^2 g^{-1} and 0.27 cm^3 g^{-1} for pure Mn_2O_3. The incorporation of Cu in Mn_2O_3 induces a great evolution of the pore size distribution. From the size distribution in inset of Figure 8b, it is shown that the size of most of the pores is 57.2, 62.4, 68.3, and 76.3 nm. The specific surface area and the pore volume can reach 18.86 m^2 g^{-1} and 0.28 cm^3 g^{-1} for Cu-doped Mn_2O_3 sample, respectively. The higher specific surface area of the Cu doped Mn_2O_3 material can be attributed to the hollow structures and will be useful to enhance the lithium storage performance of the Cu-doped Mn_2O_3 samples.

3.2. Electrochemical Characterization of the Mn_2O_3 Samples. To examine the applicability of the synthesized manganese oxide samples as anode materials for LIBs, the electrochemical performance of the anode materials was investigated. Figure 9 shows profiles for the voltage versus capacity of the 1st, 2nd, 5th, 10th, and 50th cycle of the synthesized samples at a voltage window from 0.01 to 3 V at a current density of 100 mA g^{-1}. For the pure Mn_2O_3 sample (Figure 9a), the first discharge and charge capacities are 1567 and 942 mA h g^{-1}, respectively, corresponding to a Coulombic efficiency of about 60.1%. As for the Cu-doped Mn_2O_3 sample (Figure 9b), the first discharge and charge capacities are 1998 and 1190 mA h g^{-1} respectively, with a Coulombic efficiency of about 60%. The irreversible capacity for the Mn_2O_3 material in the first cycle is attributed mainly to the formation of Li_2O, solid electrolyte interface (SEI) layer, and electrolyte decomposition. In the second cycle, the discharge capacity of pure Mn_2O_3 is 894 mA h g^{-1}, and the charge capacity is 833.8 mA h g^{-1}, corresponding to a Coulombic efficiency of 93.3%. As for the Cu-doped Mn_2O_3 microsphere sample, the second discharge capacity and charge capacity are 1066.5 and 1021.4 mA h g^{-1}, respectively, and the Coulombic efficiency can reach

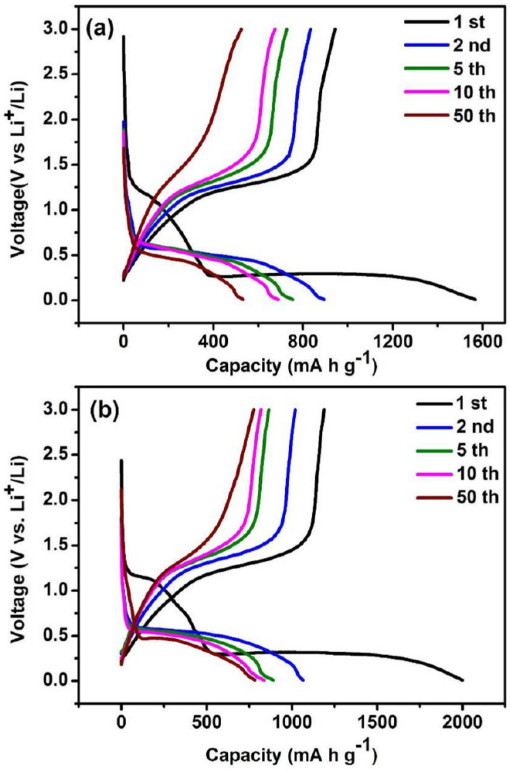

Figure 9. Discharge−charge profiles of electrode at a current density of 100 mA g^{-1} in the voltage range 0.01−3.00 V versus Li^+/Li: (a) pure Mn_2O_3 sample and (b) Cu doped Mn_2O_3 sample.

a value of up to 95.8%. After 50 discharge−charge cycles, it exhibits a high reversible capacity of 778.1 mA h g^{-1} for the Cu-doped Mn_2O_3 electrode, and the Coulombic efficiency rapidly rises to 99.7% from an initial Coulombic efficiency of 60%. In contrast, the pure Mn_2O_3 electrode only exhibits a reversible capacity of 526.8 mA h g^{-1} after 50 cycles, and the Coulombic efficiency rises to 98.9% after 50 cycles. It is obviously indicated that the Cu doped Mn_2O_3 electrode displays a much higher reversible capacity than the pure Mn_2O_3 electrode.

To understand the redox reactions of the synthesized Mn_2O_3 samples, the CV curves for the first five cycles of the pure Mn_2O_3 and Cu-doped Mn_2O_3 samples were investigated at a scan rate of 0.1 mV s^{-1} in the voltage range of 0.01−3.00 V versus Li/Li^+ (Figure 10). For the pure Mn_2O_3 sample, two reduction peaks located at 1.10 and 0.03 V are observed in the first cycle, respectively. Corresponding to the profiles for the voltage versus capacity, the peak at 1.10 V observed in the first discharge CV is attributed to the formation of the SEI layer related to the electrochemical lithium insertion reaction, and is believed to be irreversible (eqs 1 and 2). Another reduction peak at about 0.03 V can be attributed to the reduction action of Mn^{2+} to Mn^0 (eq 3). In the first anodic sweep, one peak is observed at 1.48 V, indicating the lithium extraction reaction of Li_2O during the cathodic sweep, corresponding to the reverse process of eq 3.[26]

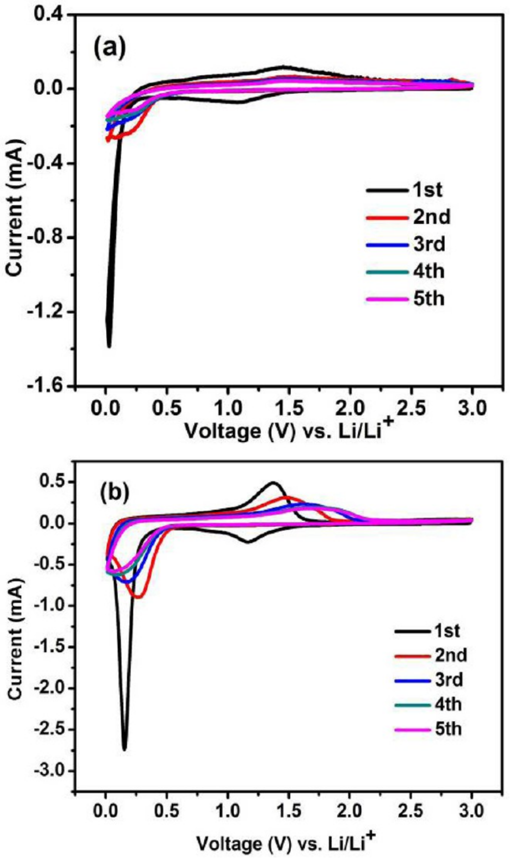

Figure 10. CV curves of the first five cycles for (a) the pure Mn_2O_3 sample and (b) Cu doped Mn_2O_3 sample electrodes at a scan rate of 0.1 mV s^{-1} between 0.01 and 3.0 V.

For the CV curve of the Cu-doped Mn_2O_3 sample, two reduction peaks located at 1.17 and 0.16 V are observed in the first cycle, respectively, which are believed to be associated with the formation of the SEI layer related to the electrochemical lithium insertion reaction (eqs 1 and 2), and the reduction action of Mn^{2+} to Mn^0 electrochemical reaction (eq 3). The oxidation peak at 1.38 V corresponds to the lithium extraction reaction of Li_2O. From the second cycle, both the pure Mn_2O_3 and Cu-doped Mn_2O_3 samples exhibit a similar trend. In the second cycle, it is noted that the reduction peak shifted to 0.16 and 0.26 V for the pure Mn_2O_3 and Cu doped Mn_2O_3 electrode, respectively.[6] After the fifth cycle, the pure Mn_2O_3 oxidation peak appeared at about 1.50 V, while the Cu doped Mn_2O_3 shifted to 1.7 V at the fifth cycle.[24] After the first cycle, the CV curves of the pure Mn_2O_3 and Cu-doped Mn_2O_3 electrodes in the second cycle remain similar to the first cycle, and the curves from the second to the fifth cycle are nearly overlapped, suggesting an excellent cyclability of the electrodes. It should be pointed that the reduction and oxidation peaks of the Cu-doped Mn_2O_3 sample is sharper than that of pure Mn_2O_3 sample, suggesting a higher activity for Cu-doped Mn_2O_3 than pure Mn_2O_3 samples.

$$2Li^+ + 3Mn_2O_3 + 2e^- \rightarrow 2Mn_3O_4 + Li_2O \qquad (1)$$

$$2Li^+ + Mn_3O_4 + 2e^- \rightarrow 3MnO + Li_2O \qquad (2)$$

$$MnO + 2Li^+ + 2e^- \leftrightarrow Li_2O + Mn \qquad (3)$$

Galvanostatic technique was utilized to investigate the charge−discharge cycling performance of the Mn_2O_3 electrodes. The core−shell structured bixbyite Mn_2O_3 displays a high specific capacity of 361 mA h g^{-1} at a high current density of 100 mA g^{-1} after 100 cycles, as shown in Figure 11a. While the hollow Cu-doped Mn_2O_3 sample still maintains a capacity at above 642 mA h g^{-1} after 100 cycles, showing a higher capacity and a better cycle stable performance. Coulombic efficiency curves of the Mn_2O_3 and Cu doped hollow Mn_2O_3 electrodes shown in Figure 11c and d indicate that the Coulombic efficiency of the core−shell structured Mn_2O_3 electrode was up to 98% after 20 cycles. As for the Cu doped hollow structure Mn_2O_3 electrode, Coulombic efficiency can obtain 99% after 20 cycles, and remains as nearly 100% thereafter. The present electrochemical lithium capacity of Mn_2O_3 and Cu-doped hollow Mn_2O_3 materials is superior to that of the previously reported performance of Mn_2O_3 materials. For example, Qiu et al.[26] reported a discharge capacity of 380 mA h g^{-1} after 150 cycles for the straw-sheaf-shape Mn_2O_3 hierarchical structures. Shim and co-workers developed the hollow rodlike manganese oxides using bacterial templates, exhibiting a high specific capacity up to about 300 mA h g^{-1} after 10 cycles.[27]

To investigate the rate capability of the Mn_2O_3 and Cu-doped hollow Mn_2O_3 electrodes, the anodes made of the manganese oxide active materials were cycled 10 cycles at each rate from 0.1 to 1.6 C (1 C = 1018 mA g^{-1} for Mn_2O_3), as shown in Figure 11b. The discharge capacities gradually decreased with increasing of the current rate. The capacities of hollow Cu-doped Mn_2O_3 microspheres are 756 mA h g^{-1} at 0.1 C after 10 cycles, 561 mA h g^{-1} at 0.2 C after 20 cycles, 431 mA h g^{-1} at 0.4 C after 30 cycles, 303 mA h g^{-1} at 0.8 C after 40 cycles, and 167 mA h g^{-1} at 1.6 C after 50 cycles. As the current was set back to 0.1 C, the capacity was able to return to more than 705 mA h g^{-1}. The result showed that almost 93% of the capacity at 0.1 C was recovered after 60 cycles. It means that the capacity of the Cu-doped Mn_2O_3 is superior to that of the commercial graphite at the higher electrical density of 0.4 C (nearly 400 mA g^{-1}). The rate capabilities of the pure Mn_2O_3

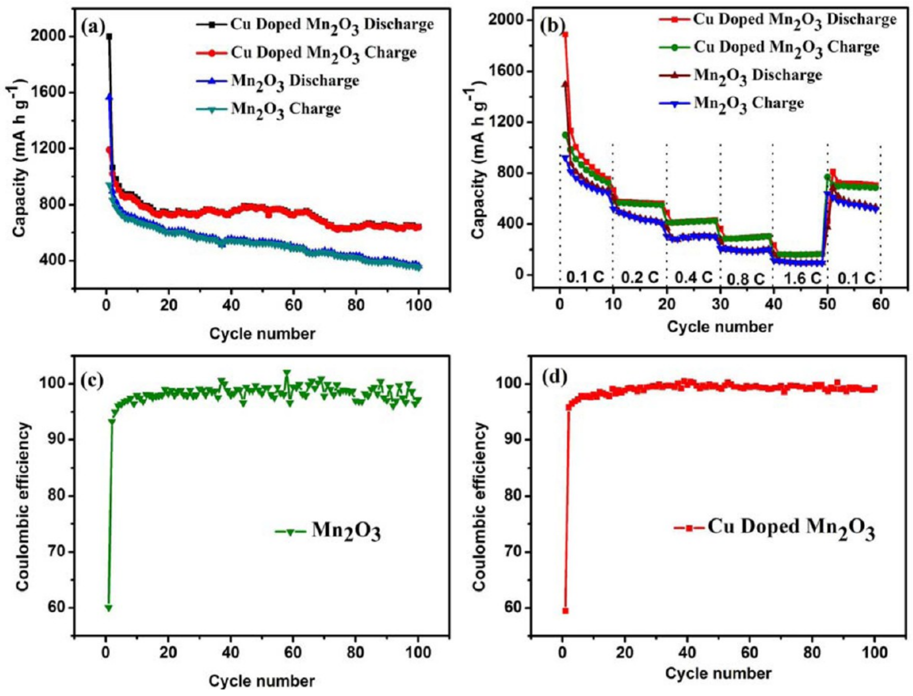

Figure 11. (a) Cyclic performance and (b) rate performances of the Mn_2O_3 samples. (c, d) Coulombic efficiency of the pure Mn_2O_3 sample and Cu doped Mn_2O_3 sample.

with discharge capacity are 664, 410, 303, 201, and 95.8 mA h g^{-1} at current densities of 0.1 C, 0.2 C, 0.4 C, 0.8C, and 1.6 C, respectively. When the current density returns back to 0.1 C, the capacity can reach 533 mA h g^{-1}. It is shown that both pure and Cu-doped Mn_2O_3 hollow spherical samples show good reversibility, and should be a great potential as an anode material in LIBs.

The electrochemical impedance spectrum (EIS) was used to investigate the charge transport kinetics for the electrochemical properties of manganese oxides samples. Figure 12 shows the Nyquist profiles of the AC impedance for pure and Cu-doped Mn_2O_3 hollow spherical samples, which were measured at an open circuit voltage state using fresh cells. In the EIS spectra, the semicircle in the high and middle frequency regions was attributed to the SEI film and charge-transfer impedance on electrode−electrolyte interface (R_{ct}), whereas the inclined line in low frequency region of the spectrum was ascribed to the mass transfer process (Warburg, R_w), which is attributed to the diffusion of Li^+ into the bulk of the electrode materials. The semicircle for Cu doped Mn_2O_3 sample was much smaller than that of pure Mn_2O_3 sample, indicating that the incorporation of Cu into Mn_2O_3 can greatly improve the charge transfer ability of Li^+ ions at the interface between the electrolyte and electrode and the conductivity of the electrode.[39−41]

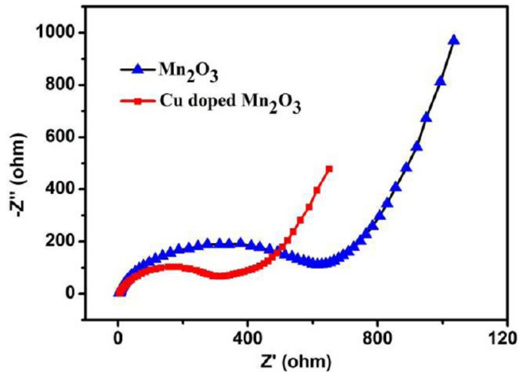

Figure 12. Nyquist plot of the synthesized samples.

The remarkable electrochemical performance, especially the high specific capacity and enhanced cycling stability of the synthesized materials, should be associated with the advantageous structure of the core−shell and hollow structures of the Mn_2O_3 and Cu-doped Mn_2O_3 spheres. (1) EIS spectra indicate that the incorporation of Cu into Mn_2O_3 can greatly improve the charge transfer ability of Li^+ ions at the interface between the electrolyte and electrode and the conductivity of the electrode.[14−18] (2) The hollow structured Cu-doped Mn_2O_3 microspheres formed by a self-supported transformation route should have high structural integrity. SEM images show that the synthesized hollow structured manganese oxide microspheres are composed of highly crystalline nanoparticles. The nanoparticle building blocks and the hollow interior can provide efficient transport of Li^+ ions because of the short diffusion length and the high porosity. (3) The hollow Cu-doped Mn_2O_3 microsphere possesses a higher specific surface area with 18.86 m^2 g^{-1}, which can offer more active sites and enhance Cu-doped Mn_2O_3 material lithium storage performance. (4) The mesoporous hierarchical core−shell and hollow microsphere structures not only provide an elastic buffer space to accommodate the volume expansion/contraction of Mn_2O_3 nanoparticles during Li^+ ions insertion/extraction process, but also efficiently prevent the aggregation of Mn_2O_3 nanoparticles and the cracking or crumbling of electrode material upon continuous cycling, thus maintaining large specific capacity, good Coulombic efficiency, high rate capability and cycling stability.[42] The SEM images of the mesocrystal hierarchical microsphere after 20 cycles at the current density of 100 mA g^{-1} shown in Figure S3 clearly indicate that the manganese oxide material can well retain the spherical morphology.

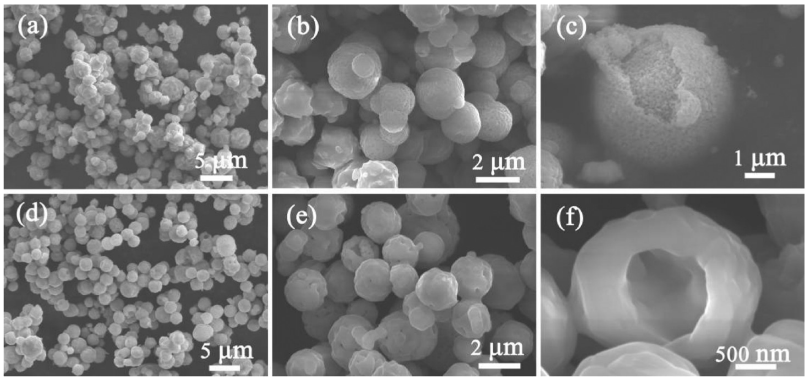

Figure 13. SEM images of pure Mn_3O_4 samples (a−c) and Cu doped Mn_3O_4 samples (d−f).

As is known, the implementation of manganese oxide in rechargeable LIBs is hampered by some practical problems, such as poor cycling performance and poor electronic conductivity. The poor cycling performance results from the large specific volume change formed during lithiation and delithiation cycling. Hollow porous nanostructured Cu-doped materials can suppress volume changes and resulting pulverization. Cationic doping has been certified to be an effective mean to improve the electrical conductivity and charge transfer ability of the anode materials.

Due to the hollow mesoporous structure and the enhancement of charge transfer ability of Li^+ ions at the interface between the electrolyte and electrode and the conductivity of the electrode induced by the incorporation of Cu in the lattice of manganese oxide, it is shown that the hollow Cu-doped manganese oxide display improved electrochemical performance compared with pure manganese oxide. Although there still shows capacity fading and relatively poor rate performance for the hollow Cu-doped manganese oxides, the electrochemical performance of the electrode materials may be further enhanced by increasing electrical conductivity by making a hybrid between the hollow Cu-doped manganese oxide and carbonaceous materials.

3.3. Structure and Electrochemical Performance of the Mn_3O_4 Samples. Figure S4 depicts the XRD patterns of the Mn_3O_4 samples obtained via thermally annealing $MnCO_3$ precursors in the presence of nitrogen gas flow.[13] It is clearly shown that the products are composed of hausmannite Mn_3O_4 with tetragonal structure (space group *I*41/*amd*) with lattice constants of a = 5.76 Å and c = 9.47 Å (JCPDS 24-0734). Figure 13 depicts SEM images of pure Mn_3O_4 samples and Cu doped Mn_3O_4 samples. Figure 13a−c gives FESEM images of the pure Mn_3O_4 samples, suggesting the core−shell structure of the synthesized products. For the Cu-doped Mn_3O_4 samples, the hollow structural nature can be clearly revealed, as shown in Figure 13d−f. Figure S5 shows the nitrogen adsorption−desorption isotherms and the corresponding pore size distribution for Mn_3O_4 samples. The specific surface area and the pore volume of the pure Mn_3O_4 and Cu doped Mn_3O_4 are 0.239 and 2.20 $m^2\ g^{-1}$, and 0.06 and 0.05 $cm^3\ g^{-1}$, respectively. The pore size distribution in Figure S5 shows that a pore structure evolution takes place from mesoporous nature for Mn_2O_3 samples to macroporous nature for Mn_3O_4 samples.

Figure 14 shows the cycling performance curves of the Mn_3O_4 and Cu-doped Mn_3O_4 samples, indicating that the electrochemical lithium storage performance of the Cu-doped Mn_3O_4 sample is better than that of the pure Mn_3O_4 sample. After 100 cycles, the pure Mn_3O_4 microsphere anode material can maintain at a value of about 327 mA h g^{-1} at the current density of 100 mA g^{-1}, whereas the Cu-doped Mn_3O_4 microsphere material displays a capacity of 400 mA h g^{-1}, corresponding to a retention 42.7% of theoretical capacity. Though the Mn_3O_4 microsphere materials showed the good lithium storage performance, it is lower than that of Mn_2O_3 materials. The possible reasons could be summarized as following. The theoretical specific capacity of Mn_3O_4 (936 mA h g^{-1}) is smaller than that of the Mn_2O_3 samples (1018 mA h g^{-1}), the smaller specific surface area of the Mn_3O_4 sample will decrease the active sites, and the macropoous structure of Mn_3O_4 is not helpful to improve the electrochemical lithium storage performance compared with the mesoporous structure for the Cu-doped Mn_2O_3 samples.

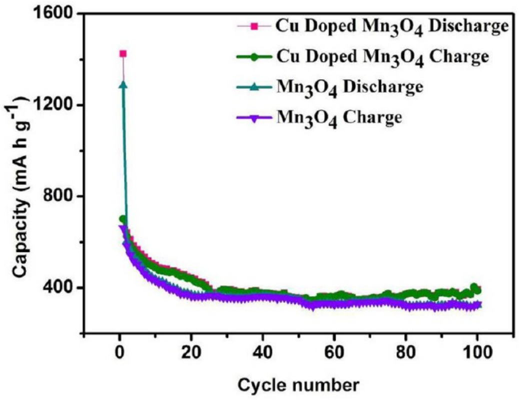

Figure 14. Cycling performance of the Mn_3O_4 and Cu-doped Mn_3O_4 samples.

4. CONCLUSIONS

We developed a facile route to prepare core−shell structure manganese oxide microsphere and Cu-doped hollow structure manganese oxide microspheres. It is found that incorporation of Cu into manganese oxide is an effective method to modulate crystal structure, morphology, surface area, and electrochemical lithium storage. Cyclic voltammetry and galvanostatic charge/discharge experiments were carried out to evaluate the electrochemical behaviors of the synthesized core−shell structured Mn_2O_3 and Mn_3O_4 materials and hollow structured Cu-doped Mn_2O_3 and Mn_3O_4 materials. The Cu-doped Mn_2O_3 hollow microspheres display the largest specific capacity with 642 mA h g^{-1} at the current density of 100 mA g^{-1} after 100 cycles, and good cycle stable performance, displaying 99%

Coulombic efficiency after 20 cycles. The improvement of the electronic conductivity and lithium diffusivity of electrodes is the major reason for the enhancement of the electrochemical lithium storage performance. At the same time, the higher specific surface area and the hollow interior of the products will also buffer the large volume change, which will enhance the cycle stable performance of the Cu-doped manganese oxide microspheres products. The capacity of the Mn_3O_4 microspheres is relatively lower than the Mn_2O_3 microspheres, due to the low theoretical capacity and small specific surface area. The manganese oxides microsphere material can find potential applications as anode material in lithium ion batteries.

■ ASSOCIATED CONTENT

Ⓢ Supporting Information

SEM images of $MnCO_3$ precursor samples, EDS spectrum of pure Mn_2O_3 microsphere, morphological analysis of the pure Mn_2O_3 sample and Cu-doped Mn_2O_3 sample after 20 cycles, XRD patterns of Mn_3O_4 materials, Nitrogen adsorption−desorption isotherms and the corresponding pore size distribution for Mn_3O_4samples. This material is available free of charge via the Internet at http://pubs.acs.org.

■ AUTHOR INFORMATION

Corresponding Author

*Tel: + 86 531 88396970. Fax: + 86 531 88396970. E-mail: yinlw@sdu.edu.cn.

Notes

The authors declare no competing financial interest.

■ ACKNOWLEDGMENTS

We acknowledge support from the National Natural Science Funds for Distinguished Young Scholars (No. 51025211), The National Basic Research Program (No. 2013CB934303), National Nature Science Foundation of China (No. 51272137), and the Tai Shan Scholar Foundation of Shandong Province.

■ REFERENCES

(1) Armand, M.; Tarascon, J. M. *Nature* **2008**, *451*, 652−657.

(2) Dunn, B.; Kamath, H.; Tarascon, J. M. *Science* **2011**, *334*, 928−935.

(3) Yu, X. Q.; He, Y.; Sun, J. P.; Tang, K.; Li, H.; Chen, L. Q.; Huang, X. J. *Electrochem. Commun.* **2009**, *11*, 791−794.

(4) Xu, G. L.; Xu, Y. F.; Sun, H.; Fu, F.; Zheng, X. M.; Huang, L.; Li, J. T.; Yang, S. H.; Sun, S. G. *Chem. Commun.* **2012**, *48*, 8502−8504.

(5) Zhou, L.; Wu, H. B.; Zhu, T.; Lou, X. W. *J. Mater. Chem.* **2012**, *22*, 827−829.

(6) Li, Z.; Liu, N.; Wang, X.; Wang, C.; Qi, Y.; Yin, L. *J. Mater. Chem.* **2012**, *22*, 16640−16648.

(7) Zhu, J.; Yin, Z.; Yang, D.; Sun, T.; Yu, H.; Hoster, H. E.; Hng, H. H.; Zhang, H.; Yan, Q. *Energy Environ. Sci.* **2013**, *6*, 987−993.

(8) Xiong, S.; Chen, J. S.; Lou, X. W.; Zeng, H. C. *Adv. Funct. Mater.* **2012**, *22*, 861−871.

(9) Wang, X.; Li, X.; Sun, X.; Li, F.; Liu, Q.; Wang, Q.; He, D. *J. Mater. Chem.* **2011**, *21*, 3571−3573.

(10) Wang, Y.; Su, D.; Ung, A.; Ahn, J.; Wang, G. *Nanotechnology* **2012**, *23*, 055402.

(11) Luo, W.; Hu, X.; Sun, Y.; Huang, Y. *J. Mater. Chem.* **2012**, *22*, 8916−8921.

(12) Poizot, P.; Laruelle, S.; Grugeon, S.; Dupont, L.; Tarascon, J. M. *Nature* **2000**, *407*, 496−499.

(13) Wang, C. B.; Yin, L. W.; Xiang, D.; Qi, Y. *ACS Appl. Mater. Interfaces* **2012**, *4*, 1636−1642.

(14) Li, J.; Xiong, S.; Li, X.; Qian, Y. *Nanoscale* **2013**, *5*, 2045−2054.

(15) Pasero, D.; Reeves, N.; West, A. R. *J. Power Sources* **2005**, *141*, 156−158.

(16) Luo, W.; Hu, X.; Sun, Y.; Huang, Y. *Phys. Chem. Chem. Phys.* **2011**, *13*, 16735−16740.

(17) Qie, L.; Chen, W. M.; Wang, Z. H.; Shao, Q. G.; Li, X.; Yuan, L. X.; Hu, X. L.; Zhang, W. X.; Huang, Y. H. *Adv. Mater.* **2012**, *24*, 2047−2050.

(18) Lee, J. W.; Hall, A. S.; Kim, J. D.; Mallouk, T. E. *Chem. Mater.* **2012**, *24*, 1158−1164.

(19) Wang, Y.; Chen, T. *Electrochim. Acta* **2009**, *54*, 3510−3515.

(20) Tian, B.; Xiang, H.; Zhang, L.; Li, Z.; Wang, H. *Electrochim. Acta* **2010**, *55*, 5453−5458.

(21) Sakunthala, A.; Reddy, M. V.; Selvasekarapandian, S.; Chowdari, B. V. R.; Selvin, P. C. *Energy Environ. Sci.* **2011**, *4*, 1712−1725.

(22) Mai, Y. J.; Tu, J. P.; Xia, X. H.; Gu, C. D.; Wang, X. L. *J. Power Sources* **2011**, *196*, 6388−6393.

(23) Yu, H.; Rui, X.; Tan, H.; Chen, J.; Huang, X.; Xu, C.; Liu, W.; Yu, D. Y. W.; Hng, H. H.; Hoster, H. E.; Yan, Q. *Nanoscale* **2013**, *5*, 4937−4943.

(24) Nam, K. M.; Choi, Y. C.; Jung, S. C.; Kim, Y.; Jo, M. R.; Park, S. H.; Kang, Y. M.; Han, Y. K.; Park, J. T. *Nanoscale* **2012**, *4*, 473−477.

(25) Hashem, A. M.; Abuzeid, H. M.; Narayanan, N.; Ehrenberg, H.; Julien, C. M. *Mater. Chem. Phys.* **2011**, *130*, 33−38.

(26) Qiu, Y.; Xu, G. L.; Yan, K.; Sun, H.; Xiao, J.; Yang, S.; Sun, S. G.; Jin, L.; Deng, H. *J. Mater. Chem.* **2011**, *21*, 6346−6353.

(27) Shim, H. W.; Lim, A. H.; Min, K. M.; Kim, D. W. *CrystEngComm* **2011**, *13*, 6747−6752.

(28) Li, J.; Xiong, S.; Li, X.; Qian, Y. *J. Mater. Chem.* **2012**, *22*, 23254−23259.

(29) Xing, G. Z.; Yi, J. B.; Tao, J. G.; Liu, T.; Wong, L. M.; Zhang, Z.; Li, G. P.; Wang, S. J.; Ding, J.; Sum, T. C.; Huan, C. H. A.; Wu, T. *Adv. Mater.* **2008**, *20*, 3521−3527.

(30) Audi, A. A.; Sherwood, P. M. A. *Surf. Interface Anal.* **2002**, *33*, 274−282.

(31) Yang, Z.; Zhang, W.; Wang, Q.; Song, X.; Qian, Y. *Chem. Phys. Lett.* **2006**, *418*, 46−49.

(32) Gao, S.; Yang, S.; Shu, J.; Zhang, S.; Li, Z.; Jiang, K. *J. Phys. Chem. C* **2008**, *112*, 19324−19328.

(33) Tu, K. N.; Gösele, U. *Appl. Phys. Lett.* **2005**, *86*, 093111.

(34) Zeng, H. Z. *J. Mater. Chem.* **2006**, *16*, 649−662.

(35) Zhang, L.; Wu, H. B.; Madhavi, S.; Hng, H. H.; Lou, X. W. *J. Am. Chem. Soc.* **2012**, *134*, 17388−17391.

(36) Hu, L.; Yan, N.; Chen, Q.; Zhang, P.; Zhong, H.; Zheng, X.; Li, Y.; Hu, X. *Chem.—Eur. J.* **2012**, *18*, 8971−8977.

(37) Liu, J.; Xue, D. *Adv. Mater.* **2008**, *20*, 2622−2627.

(38) Fan, H. J.; Knez, M.; Scholz, R.; Hesse, D.; Nielsch, K.; Zcharias, M.; Gösele, U. *Nano Lett.* **2007**, *7*, 993−997.

(39) Wang, G.; Liu, Z. Y.; Liu, P. *Electrochim. Acta* **2011**, *56*, 9515−9519.

(40) Wu, L.; Xiao, Q.; Li, Z.; Lei, G.; Zhang, P.; Wang, L. *Solid State Ionics* **2012**, *215*, 24−28.

(41) Zhao, S.; Bai, Y.; Zhang, W. *Electrochim. Acta* **2010**, *55*, 3891−3896.

(42) Hu, L.; Zhong, H.; Zheng, X.; Huang, Y.; Zhang, P.; Chen, Q. *Sci. Rep.* **2012**, *2*, 986.